Shock Waves (2010) 20:395–408
DOI 10.1007/s00193-010-0276-9

ORIGINAL ARTICLE

Experimental investigation of converging shocks in water with various confinement materials

V. Eliasson · M. Mello · A. J. Rosakis · P. E. Dimotakis

Received: 8 February 2010 / Revised: 26 May 2010 / Accepted: 18 August 2010 / Published online: 2 September 2010

Abstract Fluid-solid coupling typically plays a negligible role in confined converging shocks in gases because of the rigidity of the surrounding material and large acoustic impedance mismatch of wave propagation between it and the gas. However, this is not true for converging shocks in a liquid. In the latter case, the coupling can not be ignored and properties of the surrounding material have a direct influence on wave propagation. In shock focusing in water confined in a solid convergent geometry, the shock in the liquid transmits to the solid and both transverse and longitudinal waves propagate in the solid. Shock focusing in water for three types of confinement materials has been studied experimentally with schlieren and photoelasticity optical techniques. A projectile from a gas gun impacts a liquid contained in a solid convergent geometry. The impact produces a shock wave in water that develops even higher pressure when focused in the vicinity of the apex. Depending on the confining material, the shock speed in the water can be slower, faster, or in between wave speeds in the solid. For solid materials with higher wave speeds than the shock in water, regions in the water is put in tension and cavitation occurs. Materials with slower wave speeds will deform easily.

Keywords Shock focusing · Impact · Water · Solid · Schlieren · Photoelasticity

Communicated by O. Igra.

V. Eliasson · M. Mello · A. J. Rosakis · P. E. Dimotakis
California Institute of Technology,
Graduate Aerospace Laboratories, Pasadena, CA 91107, USA

Present address:
V. Eliasson (✉)
University of Southern California, Aerospace and Mechanical Engineering, Los Angeles, CA 90089, USA
e-mail: eliasson@usc.edu

1 Introduction

Converging shock waves are an important means to concentrate energy in a small region and thus potentially achieve very high pressures in the focal region. Shock focusing in gases has been studied since the early 1940s [1] and has provided many analytical, experimental and numerical challenges (see for example [2–6]). By changing the medium in which shock focusing occurs from a gas to a liquid, which in general has a higher density and speed of sound, the pressure increase generated by the shock is several orders of magnitude higher. The reference pressure can be approximated by $p = \rho c^2$ where ρ is the density, and c is the speed of sound; consequently, the reference pressure in water is about 2.5×10^4 times higher than in air. Converging shocks in water and their coupling to confining solids are of interest in many applications, such as marine structures subjected to dynamic loading events, and in the generation of high-speed liquid jets, e.g. [7–11].

Naval vessels, for example, have several convergent sections, such as rudder–hull junctions, propeller shafts, and bow thrusters. An example is shown in Fig. 1. In the event of a nearby explosion, the shock in the water can focus as it propagates into convergent marine geometries.

In the present investigation, a laboratory experiment was developed to investigate the fundamental nature of focused shocks in liquid media and the coupling to wave propagation in the confining solid structures. The specimen consists of a water-filled convergent cavity that is sandwiched between two windows and a square-shaped piston is used to seal-off the entrance to the water chamber. A schematic representation of the specimen assembly is shown in Fig. 1 with only one window depicted.

The so-called Bowden–Brunton method [12] is used to generate the shock wave in the water. A projectile launched

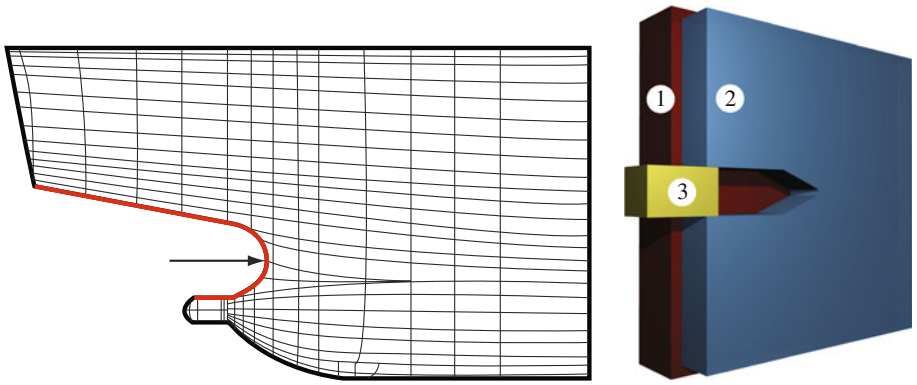

Fig. 1 Convergent section on a ship (*left*). An illustration of the sandwich structure with a water-filled wedge (*right*). *1* polycarbonate window, *2* core with water-filled wedge, and *3* piston that the projectile impacts upon

from a gas gun impacts the rear part of the piston and generates stress waves that will create a shock wave in the water. The shock generated in the water results in both pressure (longitudinal) and shear (transversal) waves in the surrounding material. In turn, the shear and pressure waves in the solid interact with the water, creating a coupled problem. Strong shock waves can be generated in the solid only if a strong enough impact is generated. In this study, schlieren diagnostics and photoelasticity techniques are used to simultaneously visualize shocks in water and air, as well as shear and pressure waves in the solid material.

The results indicate that the wave speed of the material and its relation to that in water has a significant influence on the behavior of the converging-shock process. In addition, initial findings show that depending on the type of surrounding material, cavitation can occur. If cavitation does occur, bubble collapse can further contribute to high pressures that occur during the focusing phase.

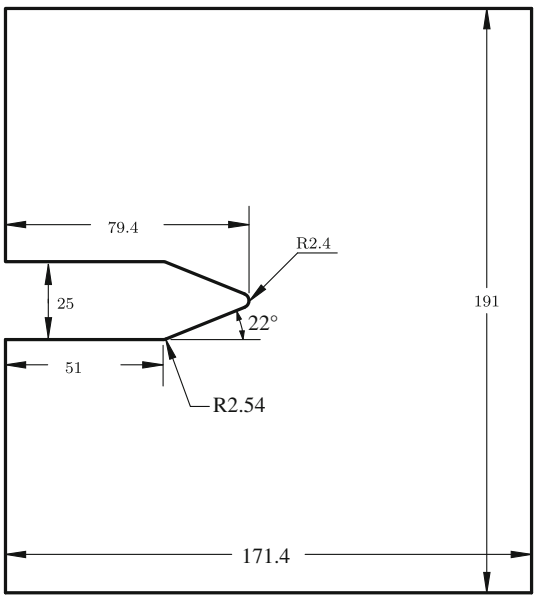

Fig. 2 Schematic of the core. Distances are given in millimeters. The thickness of the core is 25 mm

2 Experimental setup

The experimental setup consists of a single-stage gas gun, a visualization system, and the sandwich-structured specimen, as shown in Fig. 3. The core measures 171 × 191 × 25 mm^3 and contains a 22° symmetric wedge, as shown in Fig. 2. The 22° wedge is chosen based on the computer simulations performed for various wedge angles. The chosen wedge geometry assures that the reflected waves will cross each other twice and thus the pressure behind the converging shock is high. The tip radius of the wedge is set to 2.4 mm because of machining limitations. The polycarbonate windows are 38 mm thick to ensure that they remain intact. To avoid water leaking out from the water-filled wedge during the experiment, the windows are carefully sealed to the core with silicone. Precaution is taken to avoid any unintentional air bubbles in the water-filled wedge, or in the thin water film between the windows and the core. A cylindrical projectile machined out of Delrin, measuring 75 mm in length, 50 mm in diameter and with a mass of 215 g, is used to impact the polycarbonate piston. The water used in the experiments is not degassed.

The gas gun barrel is 2.1 m long with an inner bore diameter of 50.8 mm. The gun barrel is connected to a pressure chamber that generates the force to accelerate the projectile. The pressure in the chamber of the gas gun is measured with a digital pressure gauge [Druck DPI 104, absolute type, 100 psi (6.9×10^5 Pa)]. The velocity of the projectile is measured with two optical sensors in the gun barrel, placed 10.7-cm apart, with the second located 12 cm from the barrel exit. To date, the gas gun has generated impact velocities, u_i, in the range of 30–90 m/s.

The visualization system consists of a Z-folded schlieren system, and can be used simultaneously with photoelasticity techniques. The schlieren technique enables visualization of changes in index of refraction induced by compressible flows in fluids and strain fields in solids, further explained in [13]. Photoelasticity is an experimental method that enables the

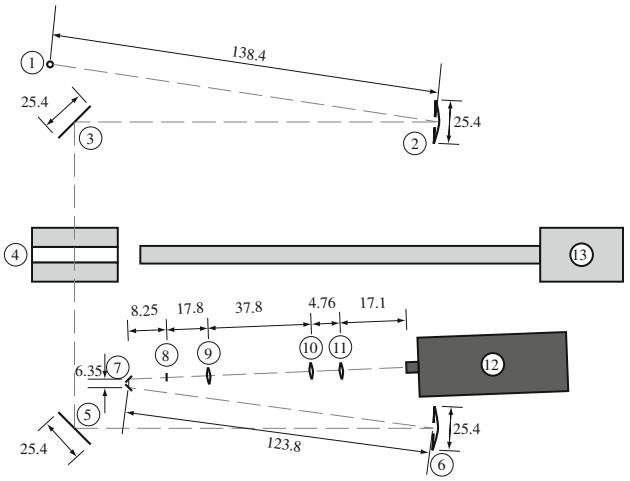

Fig. 3 An overview over the optical setup. *1* Spark source or spatial filter, *2* 25-cm spherical mirror, *3* 25-cm flat mirror, *4* sample, *5* 25-cm flat mirror, *6* 25-cm spherical mirror, *7* two mirrors, *8* knife edge or color filters, *9* 300-mm achromatic lens, *10* 200-mm achromatic lens, *11* 200-mm lens, *12* Cordin high-speed camera, *13* gas gun. The *grey dashed line* shows the light path. Distances are given in centimeters

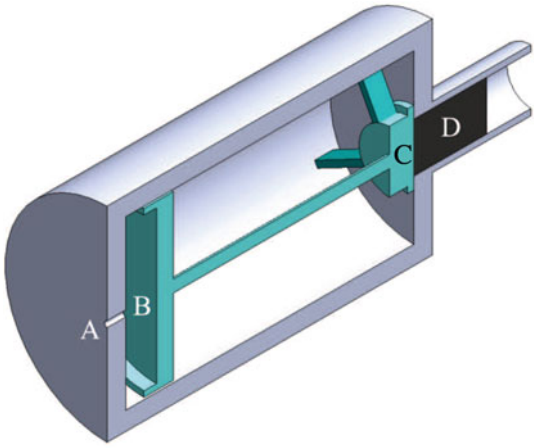

Fig. 4 A cross-section through the pressure chamber of the gas gun. **a** The rear valve location, **b** rear disc, **c** front disc and **d** projectile position before firing the gun

analysis of stress or strain fields in solid materials with birefringent properties, see for example [14,15] for a thorough explanation. Photoelasticity generates a fringe pattern based on the correlation between the indices of refraction of the material and the local in-plane principal stress components. The two-dimensional photoelastic model can be written as

$$\sigma_1 - \sigma_2 = \frac{Nf}{h}, \tag{1}$$

where σ_1 and σ_2 are the principal stresses, N is the fringe order, f is the material fringe value ($f = \lambda/C$ with λ being the wave length and C is the stress-optic coefficient), and h is the thickness of the specimen. Earlier work by Rosakis et al. on the rupture of bimaterial interfaces [16–20], represents similar and somewhat analogous investigations in the field of solid mechanics to the fluid–solid interactions addressed in this paper. Several of these studies have featured optical diagnostics, such as laser-based photoelasticity in conjunction with high-speed photography to the investigation of impact-induced mode II type dynamic ruptures along both weakly bonded bimaterial interfaces [21]. A more recent class of investigations has featured the application of dynamic photoelasticity to the characterization of mode II type ruptures along frictional interfaces with direct application to seismological problems [22,23].

The images in this study were recorded on either a high-resolution single-frame digital Nikon D80 SLR camera equipped with an AF-S Nikkor 18–135 mm zoom lens, or on a high-speed gated intensified digital CCD camera (Cordin model 214-8) capable of a total of eight frames at a sampling interval as short as 10 ns. Two different white-light sources are used for the Nikon and Cordin camera when the schlieren technique is used. The Nikon camera relies on a single spark source with a 20-ns pulse (Model 437B Nanopulser, Xenon Corporation), and the Cordin camera uses a single spark source with a 100-μs pulse (Cordin Model 673 10KV). For tests with photoelasticity, the light source consists of a continuous laser (Coherent, Verdi-V10, 10W, 532 nm).

Precise triggering of the camera and the spark source is critical because of the large difference in impact speed and wave speeds in the specimen. Triggering of the spark source is achieved via the interruption of a HeNe laser beam by the projectile as it exits the gun barrel. The resulting voltage drop from a photodetector (DET10A, 1 ns rise time) triggers a time-delay unit (BNC Model 565-4C), which sends an appropriately delayed signal to the spark source. A digital oscilloscope (LeCroy, WaveSurfer 24Xs) used to record projectile velocity and other electrical signals is simultaneously triggered. The Nikon camera shutter has no electronic triggering mechanism and the exposure time is typically set to 30 seconds in a dark-room setting with the shutter manually opened before the test. The only visible light observed during the test with the Nikon camera is the flash from the triggered spark source and the trigger beam from the HeNe laser. The short time exposure of the Cordin camera allows measurements to be recorded in ambient white light.

2.1 Gas-gun theory

Controlling the experiment is important, especially when tests must be repeated at predetermined conditions. In this section, we discuss and analyze the gun performance. A cross-section of the pressure chamber of the gun is shown in Fig. 4. The pressure chamber of the gun contains two plastic discs connected to each other. The rear disc, (B), is pulled back when gas is supplied through the rear valve (A),

and pushed forward when gas is evacuated through the same valve. When the chamber is pressurized, the disc in the front, (C), seals the exit to the gun bore. When the gun is fired, the front disc moves backward allowing the gas to flow out through the gun bore.

The acceleration and the final velocity of the projectile depends on a number of parameters, such as the pressure in the gun chamber, the mass of the bullet, and the length of the barrel. A derivation of an approximate theory for projectile velocity versus chamber pressure relations for single-stage gas guns can be found in [24]. Assuming an ideal gas, a constant diameter and infinitely long gun chamber, and an isentropic expansion behind the projectile gives an expression for the instantaneous projectile velocity, $u_{\mathrm{p}}(x,t)$, as a function of chamber pressure, p_p, and the pressure in front of the bullet p_2,;

$$m\frac{\mathrm{d}u_p(x,t)}{\mathrm{d}t} = A(p_p(u_p) - p_2(u_p)), \tag{2}$$

$$p_p(u_p(x,t)) = zp_{p1} + (1-z)p_{p2}, \tag{3}$$

where m is the mass of the projectile, x is the distance travelled by the projectile, t is the time, and A is the cross-section area of the barrel. The decrease in chamber pressure p_p depends on the pressure ratio z that is lost from the motion of the projectile and through the rear valve, modeled by (4) and (5). For (4), the assumptions are an isentropic expansion in a chamber with the same diameter as the gun barrel, given by

$$\frac{p_{p1}}{p_0} = \left(1 - \frac{\gamma-1}{2a_0}u_p\right)^{\frac{2\gamma}{\gamma-1}}, \tag{4}$$

where p_0 is the initial pressure in the gun chamber, γ is the ratio of specific heats (=1.4 for air), and a_0 is the initial speed of sound in the gun chamber. The gas escaping the chamber through the opening of the rear valve can be modeled as choked orifice flow with an finite reservoir volume given by

$$\frac{p_{p2}}{p_0} = \left(\frac{T_p(t)}{T_0}\right)^{\frac{\gamma}{\gamma-1}}, \tag{5}$$

where the temperature, $T_p(t)$, is given by

$$\frac{T_p(t)}{T_0} = \left(1 + \frac{C_1\sqrt{T_0}}{2}t\right)^{-2}, \tag{6}$$

$$C_1 = \sqrt{\gamma}\left(\frac{2}{\gamma+1}\right)^{\frac{\gamma+1}{2(\gamma-1)}}\frac{A^*}{V_d}\sqrt{R}(\gamma-1). \tag{7}$$

The derivation of (5)–(7) can be found in [25].

The pressure in front of the bullet, $p_2(u_p)$, is given by shock-wave relations and can be written as,

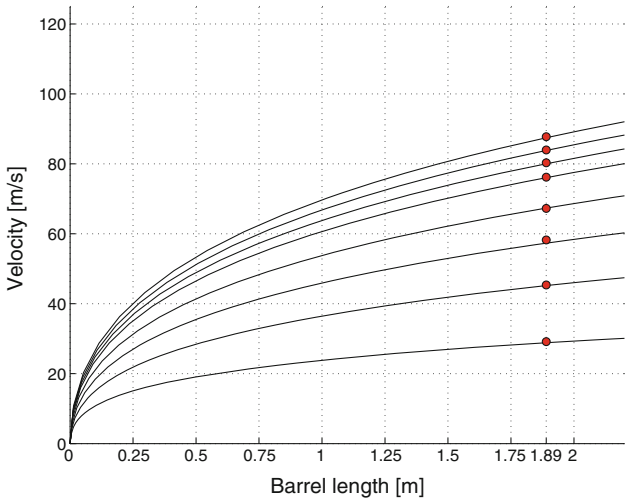

Fig. 5 Comparison between theory (*lines*) and experiments (*circular markers*) for projectile velocity for $p_0 = 30, 40, 50, 60, 70, 75, 80, 85$ psi. Location of velocity sensor, $L_0 = 1.89$ m. The size of the markers depicts the error of the measurement

$$\frac{p_2}{p_1} = 1 + \left(\frac{u_p}{a_1}\right)^2\frac{(\gamma^2+\gamma)}{4} + \frac{u_p\gamma}{a_1} \times\sqrt{1 + \left(\frac{u_p}{a_1}\right)^2\left(\frac{\gamma+1}{4}\right)^2}, \tag{8}$$

where p_2 is the pressure in front of the projectile and behind the shock wave that is launched by the projectile, a_1 and p_1 is the speed of sound and pressure in the undisturbed gas in front of the projectile, and u_{p} is the projectile velocity (the speed of the contact surface behind the shock wave).

A comparison between the theory and the experiments for the velocity of the projectile versus the barrel length is shown in Fig. 5.

2.2 Shock-reflection type

When the shock wave in the water enters the converging section, in this case, the wedge with a 22° deflection angle, the resulting shock reflection type depends on the shock Mach number and the equation of state. The reflected wave can be classified either as a regular reflection or an irregular reflection. One method to find the the limit between the two types of reflections is using a pressure-deflection $(p-\theta)$ diagram. To generate a $p-\theta$ diagram, the jump conditions across the shock and an equation of state that describes the shock medium are needed. Here, we use the stiffened equation of state [26], sometimes also referred to as the Tamman equation of state to describe the shock medium (water),

$$e = \frac{p + \gamma p_\infty}{\rho(\gamma_\infty - 1)}, \tag{9}$$

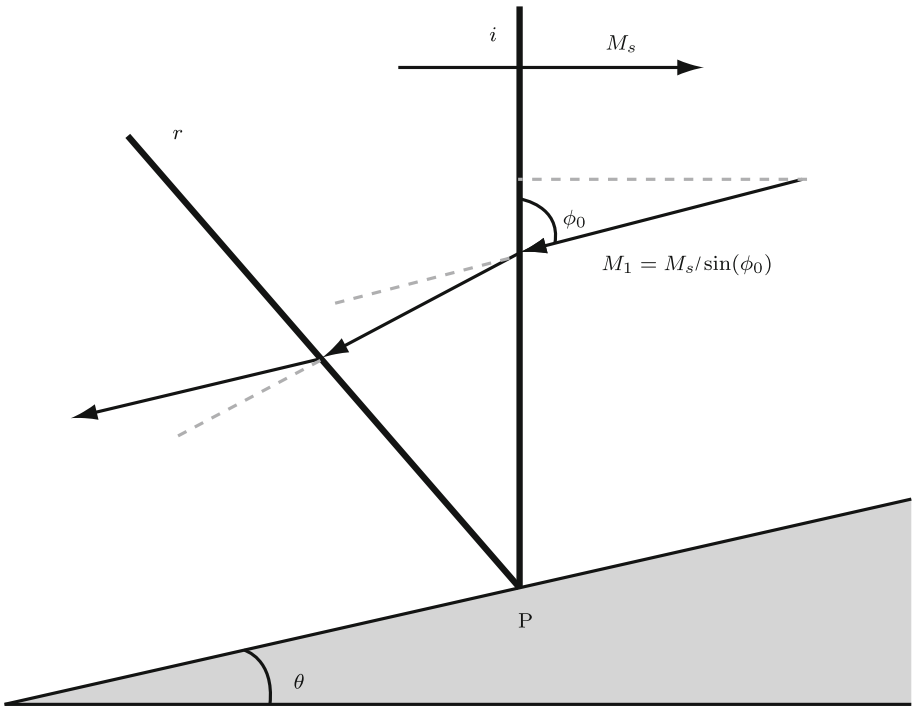

Fig. 6 An oblique non-stationary shock wave for an incident shock wave (*i*) with shock Mach number M_s, and reflected shock wave (*r*) can be made pseudo-stationary by attaching a frame of reference to the shock itself and imposing a counter flow M_1

where e is the internal energy, p is the pressure, ρ is the density, and $p_\infty = 2.962 \times 10^8$ Pa and $\gamma_\infty = 7.415$ are constants. The speed of sound corresponding to this equation of state is given by $c_w^2 = \gamma_\infty(p + p_\infty)/\rho$. The jump conditions across a shock wave for a stiffened equation of state are given by

$$\frac{u_2}{u_1} = \frac{2 + (\gamma_\infty - 1)M_1^2}{(\gamma_\infty + 1)M_1^2}, \tag{10}$$

$$\frac{\rho_2}{\rho_1} = \frac{(\gamma_\infty + 1)M_1^2}{2 + (\gamma_\infty - 1)M_1^2}, \tag{11}$$

$$\frac{p_2}{p_1} = 1 + \frac{2\gamma_\infty}{\gamma_2 + 1}(M_1^2 - 1)\left(1 + \frac{p_\infty}{p_1}\right). \tag{12}$$

Jump conditions for the density and the velocity remain the same as for jump conditions for an ideal gas. The density jump can also be expressed in terms of the pressure jump as

$$\frac{\rho_2}{\rho_1} = \frac{p_2(\gamma_\infty + 1) + p_1(\gamma_\infty - 1) + 2\gamma_\infty P_s}{p_2(\gamma_\infty - 1) + p_1(\gamma_\infty + 1) + 2\gamma_\infty P_s}, \tag{13}$$

see, for example, Saito et al. [27], for a derivation of (13). In addition, the shock is non-stationary and this has to be taken into consideration when generating the $p-\theta$ diagram. If the incident shock is moving with a constant velocity, the shock can be considered from a pseudo-stationary point of view by attaching a frame of reference to the shock itself. Jones et al. [28] showed that a self-similar, non-stationary reflection can be made pseudo-stationary by imposing a counter flow $M_1 = M_s/\sin(\phi_0)$, where $\phi_0 = 90° - \theta$, with respect to the reflection point P (see Fig. 6). The counter flow will be parallel to the wall for regular reflections and parallel to the triple point path for Mach reflection. The shock reflection domains for air represented by an ideal gas equation of state with $\gamma = 1.4$ and for water represented by a stiffened equation of state with $\gamma = 7.415$ are shown in Fig. 7. In this plot, a rigid surface is assumed. Lines 1 (air) and 2 (water)

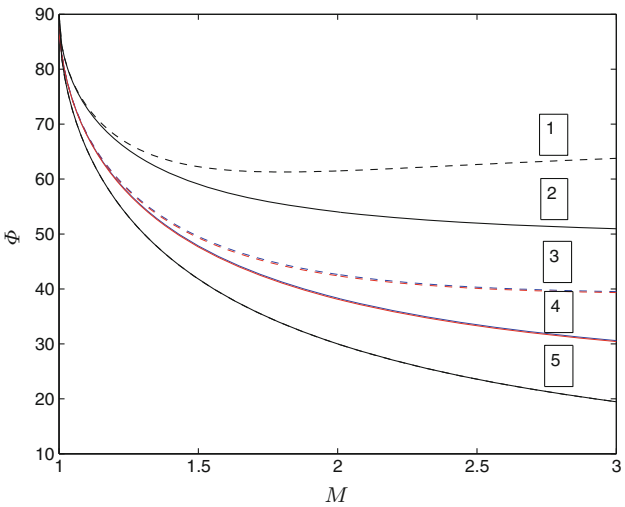

Fig. 7 Shock-reflection domain comparison between a perfect gas and a stiffened equation of state. Lines *1* and *2* show the limit for sonic flow behind the incident shock for an ideal gas with $\gamma = 1.4$ (*dashed*) and a stiffened equation of state (*solid*), lines *3* and *4* show the sonic and detachment limit for an ideal gas with $\gamma = 1.4$ (*dashed*) and a stiffened equation of state (*solid*), and line *5* is the lower limit given by the Mach wave condition and is the same for both an ideal gas and a stiffened equation of state. A rigid wedge is assumed

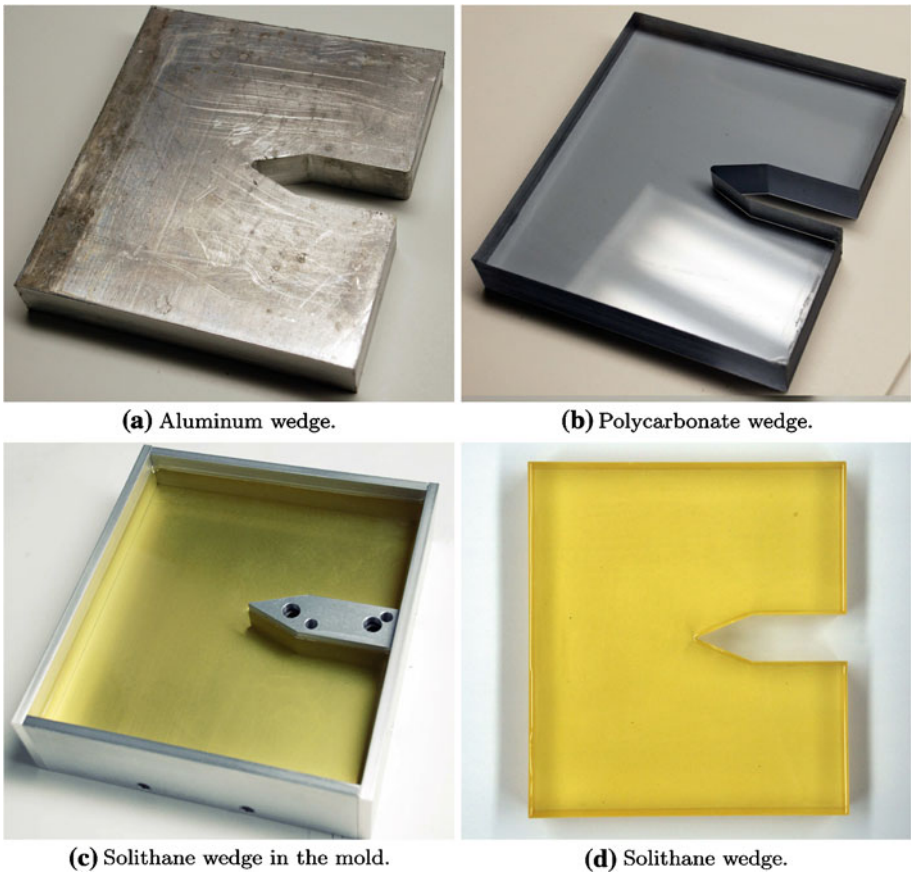

(a) Aluminum wedge. **(b)** Polycarbonate wedge.

(c) Solithane wedge in the mold. **(d)** Solithane wedge.

Fig. 8 Three types of confinement materials have been used: aluminum, polycarbonate and Solithane

represent the upper limit, where the flow behind the incident shock is sonic, and hence no reflections can occur above this line. Lines 3 (air) and 4 (water) shows the detachment and sonic lines. In this plot, the detachment line and the sonic line are close and difficult to distinguish from each other. The detachment line is where the deflection angle for the reflected shock takes its maximum value. The sonic line represents the state where the Mach number behind the reflected shock is sonic and this is usually given as the transition criterion between a regular and irregular reflection [29]. The lower limit for the reflection domain is given by the Mach wave condition $\phi = \sin^{-1}(1/M)$, line 5, and is the same for both air and water. Only points on or above this line can give an incident shock. A thorough discussion of the shock-reflection domain for an ideal gas can be found in [30].

2.3 Three types of confinement material

Experiments have been performed for three types of confinement materials: rubber (Solithane), plastic (polycarbonate) and metal (aluminum) (see Fig. 8). The aluminum and polycarbonate are machined into the correct shape, while the Solithane is cast in a mold and cured in an oven for several days.

The three materials are chosen such that the shock speed in the water, u_s, is lower, in between, or higher than the wave speeds, c_s and c_p, in the solids, respectively. In Case I, with an aluminum core, the shock speed is lower than both the shear and pressure wave speed: $u_s < c_s < c_p$. The shear (s) and pressure (p) waves propagate faster than the shock wave in the water. Theoretically, this produces two oblique shocks in the water, θ_{wp} and θ_{ws}, as shown in Fig. 9. The angles of the oblique shocks are given by $\theta_{wp} = \arcsin(c_w/c_p)$, and $\theta_{ws} = \arcsin(c_w/c_s)$, where c_w represents the speed of sound in water. The speed of sound in pure water depends only on temperature to a good approximation, see [31,32]. In the present experiments, the ambient temperature was 23 ± 1°C, giving a speed of sound of $1{,}491 \pm 2.8$ m/s in water.

Case II corresponds to a shock speed in water larger than the s wave and slower than the p wave in the solid, $c_s < u_s < c_p$. This case was studied with the core made of polycarbonate. The s wave propagates slower than the shock wave, and p waves propagate faster. This results in one oblique shock in water and one oblique shock in the solid (see Fig. 10). The angle for the oblique shock for the s wave in the solid is given by $\theta_s \arcsin(c_s/u_s)$.

The last case, Case III, is when the shock speed in the water is larger than both the s and p wave speeds (see Fig. 11). A core made of Solithane results in this condition. The

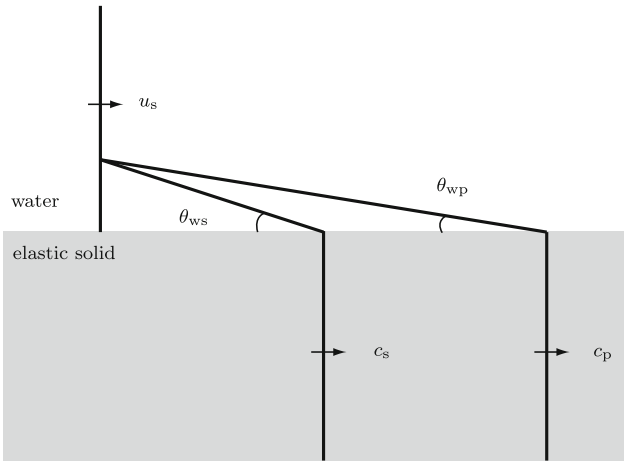

Fig. 9 Case I, the speed of the shock, u_s, is faster than both the s and p wave. The core material is aluminum

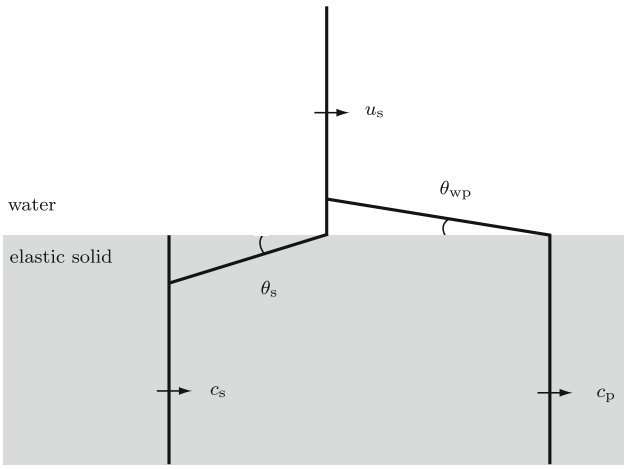

Fig. 10 Case II, the speed of the shock, u_s, is faster than the s wave and slower than the p wave. The core material is polycarbonate

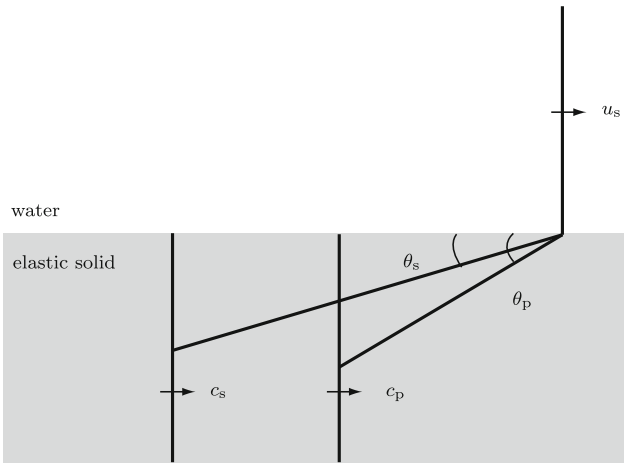

Fig. 11 Case III, the speed of the shock, u_s, is faster than both the s and p wave. The core material is Solithane

Table 1 Theoretical values of the oblique angles for Case I–III

Case	θ_{ws}	θ_{wp}	θ_s	θ_p
I	$27.7° \pm 0.5°$	$13.5° \pm 0.2°$	–	–
II	–	$45.2° \pm 3°$	$38.0° \pm 3.4°$	–
III	–	–	$3.9° \pm 0.3°$	$29.3° \pm 2.7°$

Table 2 Material properties. Pressure wave speeds are measured with an ultrasonic analyzer

	Aluminum	Polycarbonate	Solithane
c_p (m/s)	$6{,}370 \pm 120$	$2{,}100 \pm 110$	760 ± 50
c_s (m/s)	$3{,}150 \pm 60$	950 ± 50	106 ± 7
ρ (kg/m^3)	2,700	1,270	980
ν (1)	0.33	0.37	0.49
E (Pa)	7.4×10^{10}	3.2×10^9	3.3×10^7

oblique shock in the solid corresponding to the p wave is given by $\theta_p = \arcsin(c_p/u_s)$.

Theoretical values of the oblique angles for the three cases are presented in Table 1. The wave speeds for the different materials used in the experiments are presented in Table 2. The p wave speeds in the aluminum, polycarbonate, and Solithane were measured with an ultrasonic analyzer (Panametrics 5052UA), and shear-wave speeds were calculated using c_p, ρ, ν (Poisson's ratio), and E (Young's modulus).

3 Experimental results

3.1 Case I: $u_s < c_s < c_p$

A sequence of schlieren images recorded during the same experiment with the high-speed camera for the aluminum core is shown in Figs. 12 and 13. The windows are made of 38- mm-thick polycarbonate. Weak precursors of the s wave propagation in the aluminum are seen in the water in both frames reproduced in Fig. 12a and b, marked by black dotted lines in the frame reproduced in Fig. 12a. A bubble, located in the lower left corner in the frame reproduced in Fig. 12a, is oscillating in response to the passage of the shock wave. The oscillations send out compression waves, one of which is marked with an arrow in frame 12b. The shear waves in the aluminum core are traveling with almost twice the velocity of the shock wave in the water. When the shear waves passes the wedge tip, the wedge tip wants to move in the direction of the shear waves, and the resulting force on the wedge puts the water in tension. As a result, cavitation bubbles are visible in front of the shock wave in the frame reproduced in Fig. 12c. The bubbles collapse violently and disturb the wave propagation in the subsequent frames, as shown in frames 13a–c by the smudge at the interface between the water and the

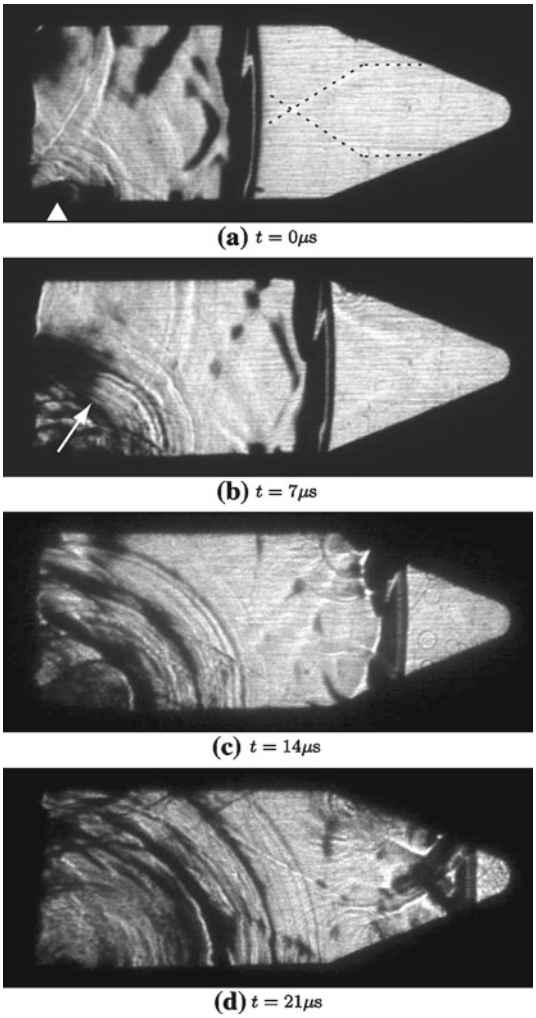

Fig. 12 A schlieren sequence for Case I. Exposure time: 200 ns. Impact speed $u_i = 45.4$ m/s

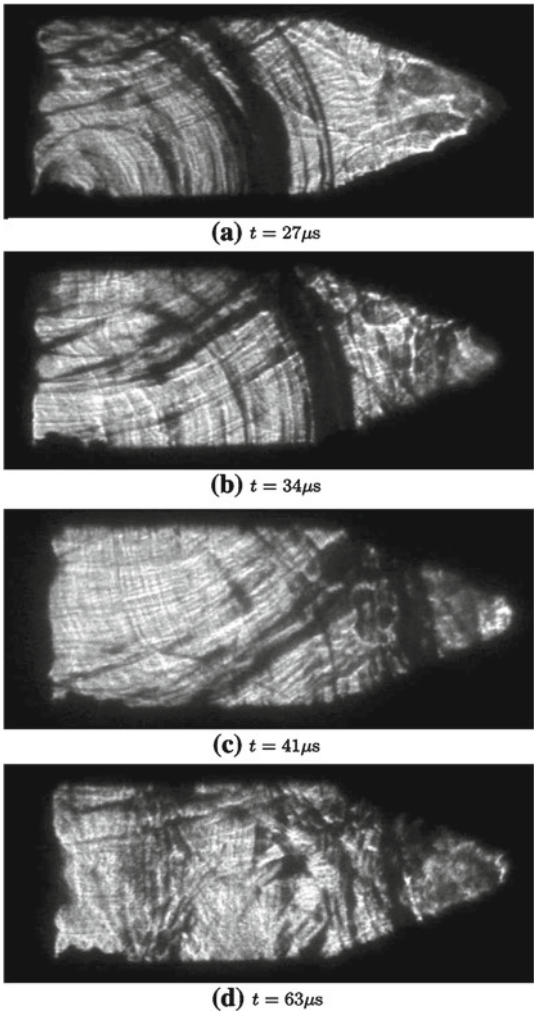

Fig. 13 A schlieren sequence for Case I. Exposure time: 200 ns. Impact speed $u_i = 45.4$ m/s

solid wedge. The shock wave has focused and is reflecting in frames 13a–d.

Schlieren images recorded using the high-speed camera with the aluminum core are shown in Fig. 14. The two frames shown in Fig. 14 are taken with 9.5- mm-thick Homalite windows. The speed of the shock wave is obtained by measuring the angle between the lower wall and the inclined shock (white line). The angles measure 16° for Fig. 14a and 29° for Fig. 14b, corresponding to shock speeds of 5,380 and 2,800 m/s, respectively, which correspond to the pressure- and shear-wave speed for aluminum (see Table 2). As seen in frame 14b, there is a black region behind the converging shock that prevents visualization of the area behind the shock. This is because the Homalite windows are thin and break, preventing light to pass through the schlieren system.

The results on shock focusing in a similar configuration using aluminum core and polycarbonate windows with a wedge angle of 19.5° have been obtained by Matthujak et al. [10]. The authors used a vertical two-stage light-gas gun to achieve projectile speeds on the order of 300 m/s [33]. Matthujak et al. visualized the wave propagation in the water-filled cavity and the 40- mm-thick windows by double-exposure holographic interferometry. The experiments showed evidence of oblique shocks in the water corresponding to the shear wave speed in the aluminum. No oblique shocks from the longitudinal wave speed were reported. An optical fiber probe hydrophone was used to measure the pressure at the apex of the converging aluminum core. Peak pressures up to 12.4 GPa were obtained by Matthujak et al. about $5.6p$ where p is the previously mentioned reference pressure $p = \rho c^2$.

3.2 Case II: $c_s < u_s < c_p$

A typical schlieren image for Case II is shown in Fig. 15. The projectile, shown moving from left to right in the image, has already impacted the polycarbonate piston. Note that the

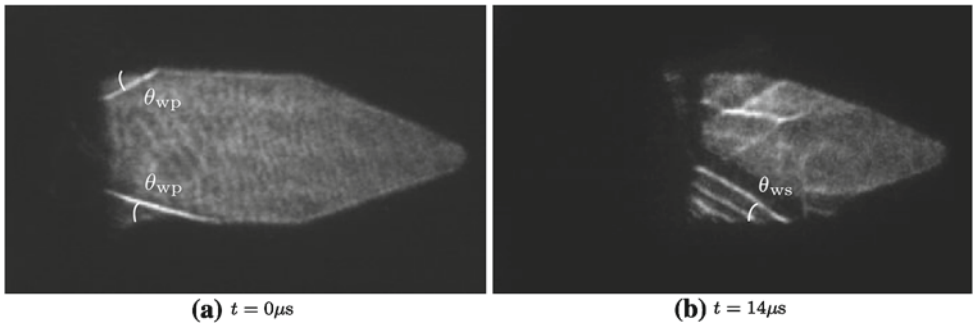

Fig. 14 Oblique precursor waves from the pressure and shear wave in the core material. Impact speed $u_i = 54.3$ m/s. Exposure time 200 ns

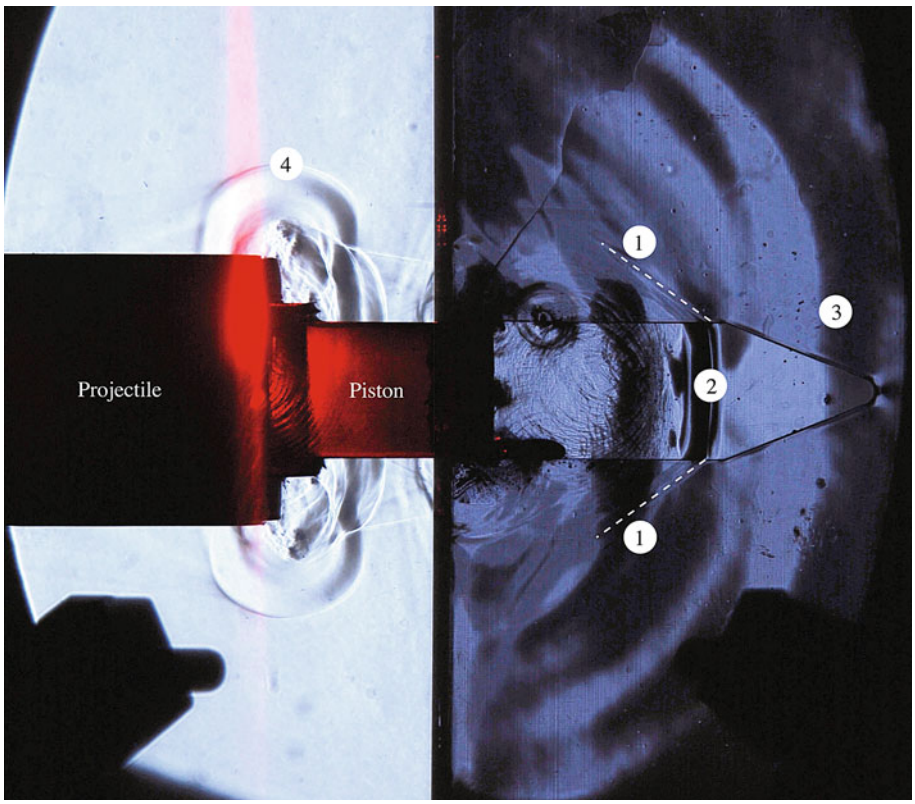

Fig. 15 Schlieren image recorded for Case II using a Nikon D80 camera and a 20-ns single spark source. *1* Oblique shear waves, *2* shock wave in water, *3* pressure wave, and *4* shock waves in air. Impact speed $u_i = 56.6$ m/s

piston is only partially inserted into the water-filled cavity as revealed by the portion, which appears black, as opposed to the portion in air that is glowing red from the scattered laser light. The red vertical streak of light shown crossing the projectile's path is the HeNe laser beam used to trigger the measurement diagnostics. The image shows waves in three separate media simultaneously: shock waves in air, shock waves in water, and shear and pressure waves in a solid.

The impact between the projectile and the piston generates a toroidal shock wave in the air. The symmetry of the upper and lower parts of the toroidal shock indicates that the impact was aligned (planar) and well controlled. Once the Mach number of the toroidal shock wave is established for a certain impact velocity, the toroidal shock can be used as an internal clock for events following, making it possible to determine the instant of the impact. The toroidal shock wave in the air (denoted as 4 in Fig. 15) has traveled a distance of 18.3 ± 0.2 mm during the impact time, t_i. The shock Mach number of $M = 1.14 \pm 0.01$ indicates a relatively weak shock wave in air.

By analyzing Fig. 15, the speed of the shock wave, u_s, propagating through the water can be estimated by measuring the Mach angle, θ_s, of the oblique shock in the polycarbonate core (denoted 1). The angle measures as $38° \pm 1°$, giving the speed of the shock in water $u_s = c_{solid}/\sin\theta = (950 \pm 50/)\sin(38° \pm 1°) = 1{,}550 \pm 88$ m/s.

The shock wave in water (denoted 2) has traveled 43 mm with a shock Mach number of $M_s = u_s/c_w = (1{,}550 \pm 88)/1{,}491 \pm 2.8 = 1.04 \pm 0.06$, which is consistent with a

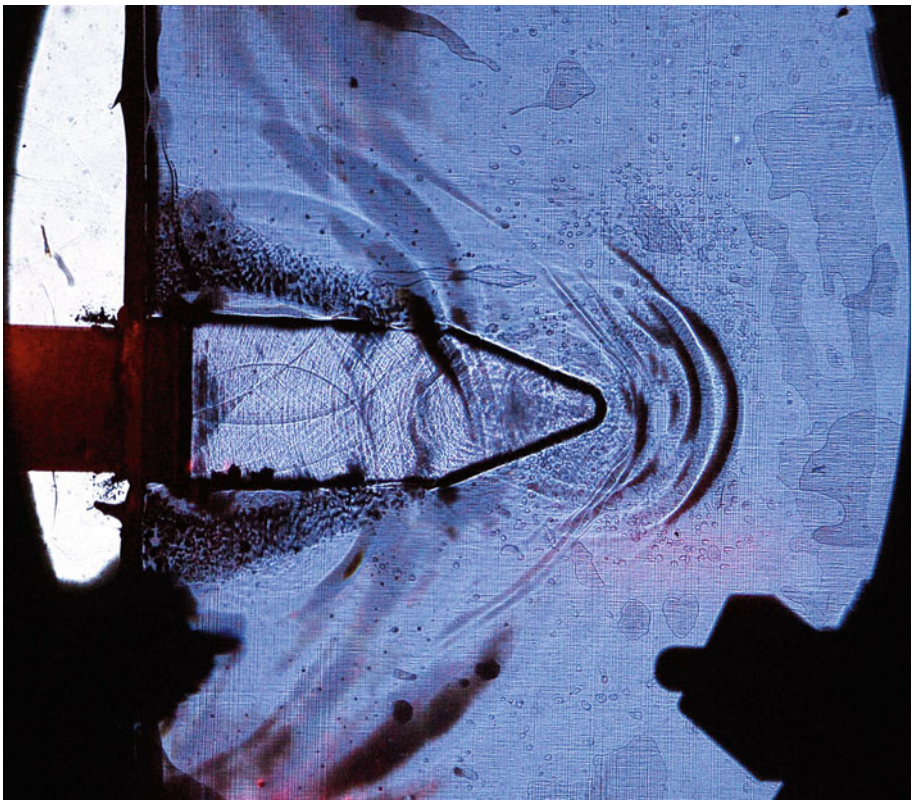

Fig. 16 Schlieren image for Case II with a Nikon D80 camera and a 20-ns single spark source. Impact speed $u_i = 44.6$ m/s

weak (acoustic) shock in water. Behind the shock in water is an intricate shock pattern consisting of a large number of circular shocks generated by collapsing bubbles induced by cavitation.

The time of impact can be estimated by following the path of the shock wave in the water. First, there is a delay set on the time-delay unit, in this case, $t_d = 94$ μs. It takes $t_p = l_p/c_p = 0.041 \pm 0.001\,\text{m}/2{,}100 \pm 100\,\text{m/s} = 19 \pm 1$ μs for the pressure wave to propagate through the piston, with length l_p, until it emerges into the water. Then, it takes $t_w = l_w/u_s = 42.7 \pm 1\,\text{mm}/1{,}550 \pm 90\,\text{m/s} = 27 \pm 1.7$μs for the shock wave to travel the distance between the end of the piston to the current position, l_w. Thus the time of impact, t_i, can be estimated as $t_i = t_d - t_p - t_w = 47 \pm 2$ μs before the time instant in the present frame. The pressure wave in the polycarbonate is too weak to generate a detectable oblique shock in the water, consequently the angle denoted θ_{wp} in Fig. 10 is not visible in the schlieren image. The pressure wave (the dark/light band denoted 3) has almost reached the tip of the wedge. As can be seen in the image data, the pressure wave has traveled 70 ± 1 mm in 27 ± 1.7 μs, corresponding to a speed of $2{,}540 \pm 160$ m/s.

A schlieren image some time after the shock wave in the water has focused and started to reflect is shown in Fig. 16. The focusing of the shock wave in water generates a strong cylindrical pressure wave in the solid. The wave pattern inside the wedge shows a pattern of several reflected shocks interacting with each other. The two cavitation zones above and below the wedge are located in the water-filled gap between the windows and the core.

A sequence of simultaneous schlieren and photoelasticity images are shown in Fig. 17. The isochromatic fringe pattern from the solid parts, the core and the two windows, overlaps with the schlieren effect. Figure 17a shows the water-filled wedge before the test and the fringe pattern in this image is from the remaining stresses caused by the manufacturing of the wedge. Figure 17b–e are taken with an interval of 10 μs. The location of the shock wave in the water is marked 's', and the pressure wave fronts in the core and windows are marked 'p'. In Fig. 17c, the angle θ_s measures $34° \pm 1°$, corresponding to a shear wave speed of 870 ± 60 m/s, which agrees well with the measured value of 954 ± 54 m/s. The upper right corner of Fig. 17c shows a blow up of the oblique waves with angle θ_s. The shock speed in the water measured on the images reproduced in frames (b) and (c) is $1{,}508 \pm 90$ m/s, frames (c) and (d) is $1{,}614 \pm 90$ m/s, and frames (d) and (e) is $1{,}570 \pm 90$ m/s. The pressure wave speed measured using frames (b) and (c), and frames (c) and (d) is 1,993 and $2{,}214 \pm 110$ m/s respectively.

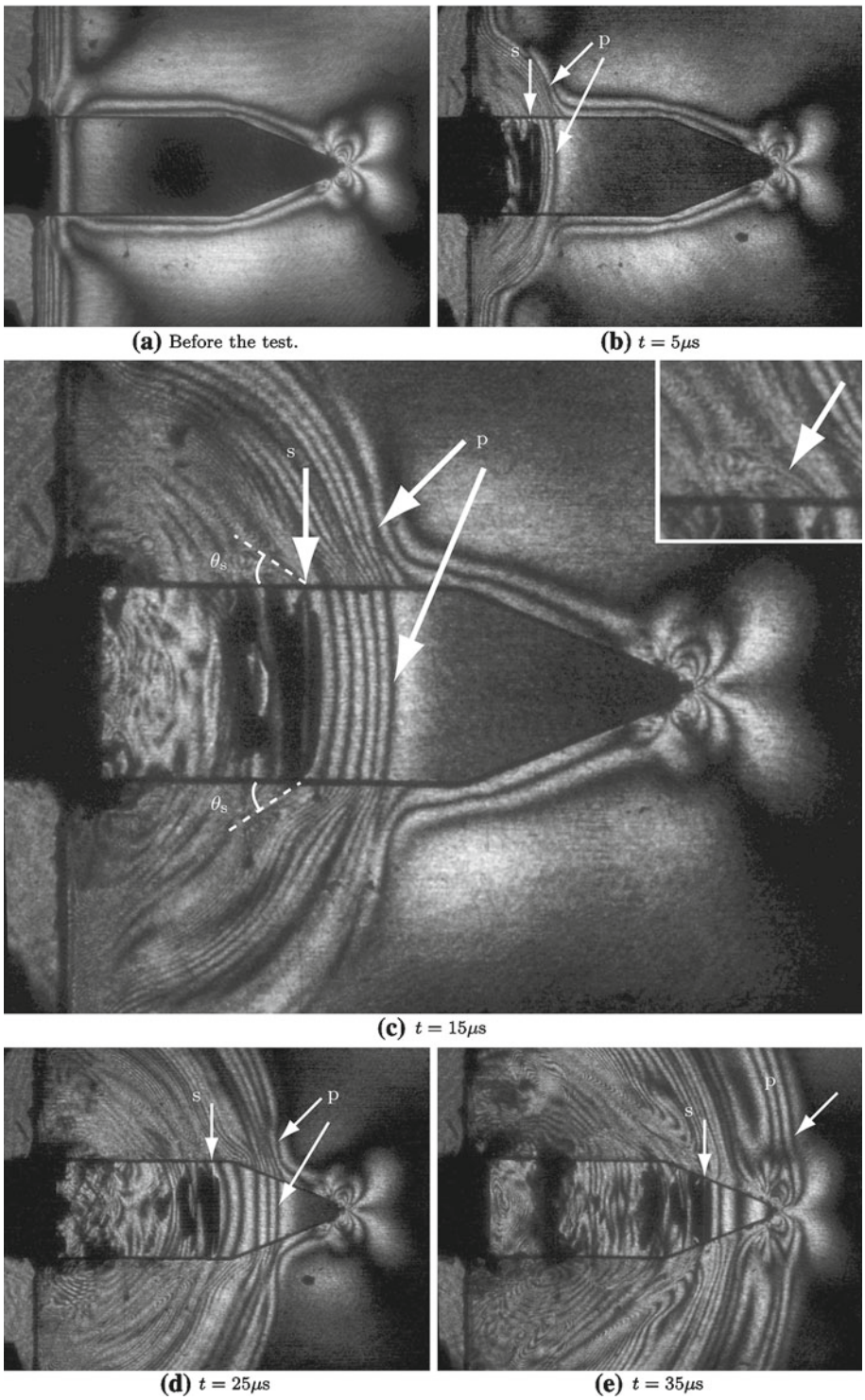

Fig. 17 A sequence of simultaneous schlieren and photoelasticity images for Case II recorded with a high-speed camera. Core and windows are made of polycarbonate. The locations of pressure waves in the polycarbonate and the shock wave in the water are indicated. Impact speed $u_i = 42.4$ m/s. Exposure time 200 ns

3.3 Case III: $c_s < c_p < u_s$

A sequence of simultaneous schlieren and photoelasticity images for a Solithane core with polycarbonate windows is shown in Fig. 18. Frame (a) in Fig. 18 shows the Solithane before impact. The dark outline of the water-filled region is caused by the manufacturing process using a mold. The isochromatic fringe pattern from the Solithane core and the polycarbonate windows overlap, creating a complex fringe pattern. The p wave propagation in the windows is faster than in the core. Measured on images reproduced in frames 18b–e, the p wave speed in the windows is $2{,}100 \pm 100$ m/s.

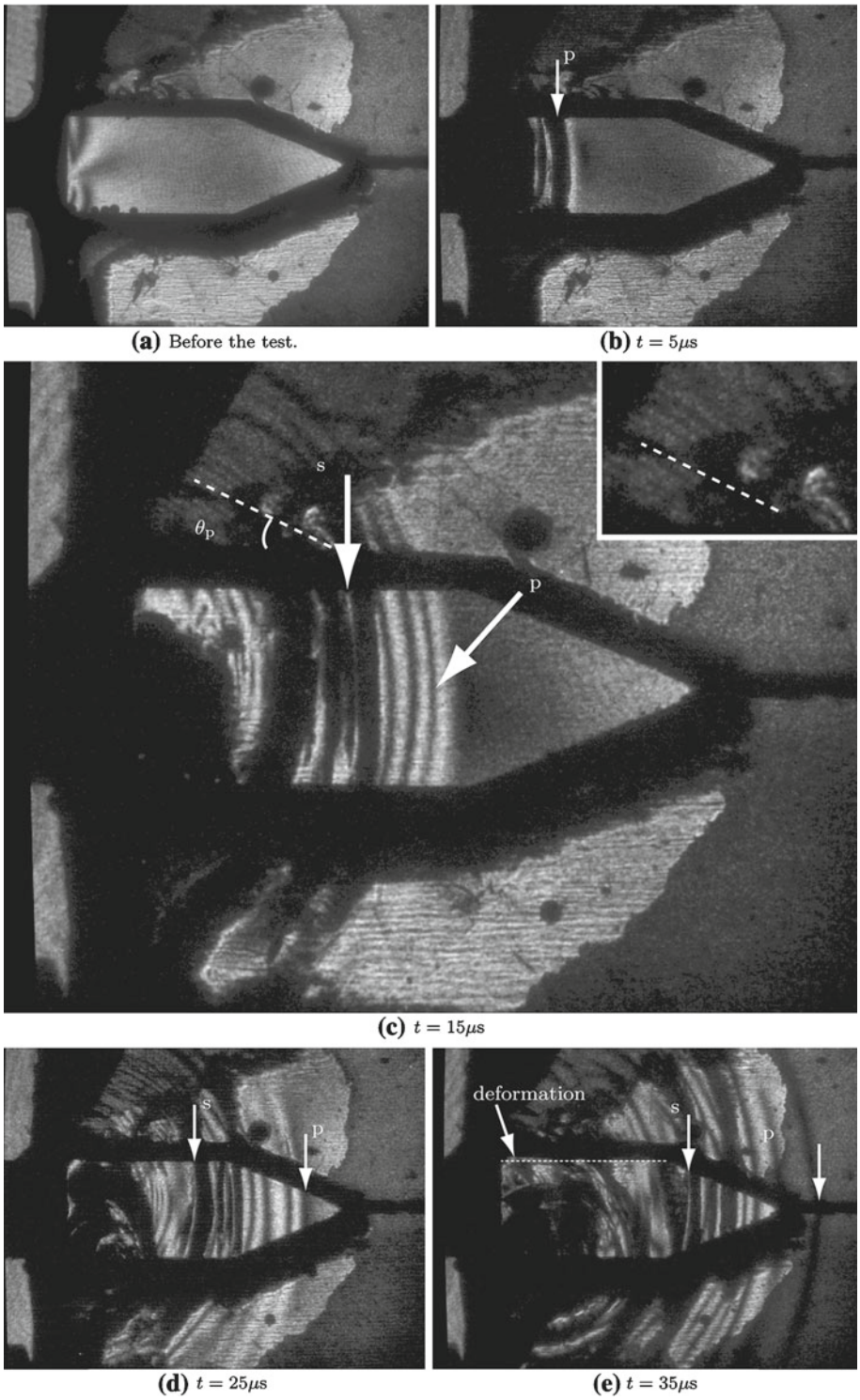

Fig. 18 A sequence of simultaneous schlieren and photoelasticity images for Case III recorded with a high-speed camera. The core is made of Solithane and the windows are made of polycarbonate. The locations of pressure waves in the polycarbonate window and the shock wave in the water are indicated. Impact speed $u_i = 46.2$ m/s. Exposure time 200 ns

The measured shock speed in the water based on frames 18b–e is 1,620 ± 90 m/s, 1,500 ± 90 and 1,630 ± 90 m/s. The angle in Fig. 18c, θ_p, is measured as 32° ± 1° that corresponds to a wave speed of 850 ± 50 m/s. This is in reasonable agreement with the p wave speed measured with the ultrasonic analyzer of 760 ± 50 m/s. The upper right corner of Fig. 18c shows a blow up of the oblique waves with angle θ_p. Solithane is a relatively soft material, and the deformation is clearly visible in the image reproduced in frame 18e.

4 Conclusions

The results presented here represent a first step in the validation of an experimental methodology for characterizing

shock focusing in converging geometries in water, and provide new information on the response of the surrounding solid material and how it affects the focusing. In addition, the present results can enable the validation of models and numerical schemes used for dynamic impact events where liquid–solid interactions are of importance.

The shock speed in the water was held constant with a Mach number of $M = 1.04 \pm 0.6$ while the longitudinal and transversal wave speeds in the surrounding solid was varied by using different materials. The shock speed in the water was lower than both the longitudinal and transverse wave speeds in the aluminum, higher than the transverse and lower than the longitudinal wave speed for polycarbonate and higher than both the transverse and the longitudinal wave speed in Solithane. For the aluminum case, precursor waves was visible in the water generated by the transverse waves in the solid. Cavitation bubbles were generated ahead of the shock in the water as a consequence of the relation between the higher waves speeds in the aluminum and the shock waves speed in the water. Both shear and pressure waves were visible in the solid core in the case with polycarbonate. As the shock wave in the water focused, a strong cylindrical pressure pulse was released from the apex of the wedge into the polycarbonate core. For the third case, the shock wave in the water generated visible oblique pressure waves in the Solithane, and the deformation of the material was clearly visible.

In the future, the experimental configuration will be modified to characterize the nature of focused shocks associated with more complex geometries. In addition, investigations will address shock-focusing effects within convergent geometries using engineering materials and shapes commonly found in marine structures and naval vessels. Further, simultaneous optical and pressure diagnostics will be implemented, thus giving quantitative results. Efforts will be undertaken to increase the shock Mach number in the water meaning that the reflection regions can be probed, and experiments can be compared to theoretical results based on a stiffened equation of state.

Acknowledgments The authors gratefully acknowledge the support of the Office of Naval Research through a MURI Grant Number N00014-06-1-0730 (Dr. Y.D.S. Rajapakse, Program Manager) to the California Institute of Technology. The authors wish to thank Dr. A.A. Shapiro at NASA/JPL for providing and preparing the Solithane cores used in the experiments, the Caltech Aero machine shop, Dr. Chris Bond, Dr. David Hill, Dr. Dan Lang, and Mr. Bahram Valiferdowsi.

References

1. Guderley, G.: Starke kugelige und zylindrische Verdichtungsstöße in der Nähe des Kugelmittelpunktes bzw. der Zylinderachse. Luftfahrt. Forsch. **19**, 302–312 (1942)
2. Perry, R.W., Kantrowitz, A.: The production and stability of converging shock waves. J. Appl. Phys **22**, 878–886 (1951)
3. Takayama, K., Kleine, H., Grönig, H.: An experimental investigation of the stability of converging cylindrical shock waves in air. Exp. Fluids **5**, 315–322 (1987)
4. Whitham, G.B.: A new approach to problems of shock dynamics. Part 1. Two-dimensional problems. J. Fluid Mech. **2**, 145–171 (1957)
5. Schwendeman, D.W., Whitham, D.W.: On converging shock waves. Proc. R. Soc. Lond. A **413**, 297–311 (1987)
6. Eliasson, V., Henshaw, W.D., Appelö, D.: On cylindrically converging shock waves shaped by obstacles. Phys. D Nonlinear Phenomena **237**, 2203–2209 (2008)
7. O'Keefe, J.D., Wrinkle, W.W., Scully, C.N.: Supersonic liquid jets. Nature **213**, 23–25 (1967)
8. Obara, T., Bourne, N.K., Field, J.E.: Liquid-jet impact on liquid and solid surfaces. Wear **186**(187), 388–394 (1995)
9. Shi, H.-H., Koshiyama, K., Itoh, M.: Further study of the generation technique of high-speed liquid jets and related shock wave phenomena using a helium gas gun. Jpn. J. Appl. Phys. **35**, 4147–4156 (1996)
10. Matthujak, A., Hosseini, S.H.R., Takayama, K., Sun, M., Voinovich, P.: High speed jet formation by impact acceleration method. Shock Waves **16**, 405–419 (2007)
11. Pianthong, K., Matthujak, A., Takayama, K., Milton, B.E., Behnia, M.: Dynamic characteristics of pulsed supersonic fuel sprays. Shock Waves **18**, 1–10 (2008)
12. Bowden, F., Brunton, J.: Damage to solids by liquid impact at supersonic speeds. Nature **181**, 873–875 (1958)
13. Settles, G.S.: Schlieren and shadowgraph techniques. In: Visualizing Phenomena in Transparent Media. Springer, Berlin (2001)
14. Frocht, M.M.: Photoelasticity. Wiley, New York (1948)
15. Dally, J.W., Riley, W.F.: Experimental Stress Analysis. McGraw-Hill, New York (1978)
16. Lambros, J., Rosakis, A.J.: Dynamic decohesion of bimaterials: experimental observations and failure criteria. In: Rosakis, A.J., Shukla, A., Rajapakse, Y.D.S. (eds.) International Journal of Solids and Structures. Special Volume devoted to dynamic failure mechanics of modern materials, vol. 32, pp. 2677–2702 (1995)
17. Lambros, J., Rosakis, A.J.: Development of a dynamic decohesion criterion for subsonic fracture of the interface between two dissimilar materials. Proc. R. Soc. Lond. **451**, 711–736 (1995)
18. Liu, C., Huang, Y., Rosakis, A.J.: Shear dominated transonic interfacial crack growth in a bimaterial-II. Asymptotic fields and favorable velocity regimes. J. Mech. Phys. Solids **43**, 189–206 (1995)
19. Rosakis, A.J., Samudrala, O., Coker, D.: Intersonic shear crack growth along weak planes. Mater. Res. Innovations **3**, 236–243 (2000)
20. Rosakis, A.J.: Intersonic shear cracks and fault ruptures. Adv. Phys. **51**, 1189–1257 (2002)
21. Rosakis, A.J., Samudrala, O., Singh, R.P., Shukla, A.: Intersonic crack propagation in bimaterial systems. In: Ravichandran, G., Rosakis, A.J., Ortiz M., Rajapakse, Y.D.S., Iyer, K. (eds.) Journal of Mechanical Physics Solids. Special Volume on dynamic deformation and failure mechanics of materials, vol. 46, pp. 1789–1813 (1998)
22. Rosakis, A.J., Xia, K., Lykotrafitis, G., Kanamori, H.: Dynamic shear rupture in frictional interfaces: speeds, directionality, and modes. Geophys. Res. Lett. **4**, 153–192 (2007)
23. Rosakis, A.J., Samudrala, O., Coker, D.: Cracks faster than the shear wave speed. Science **284**, 1337–1340 (1999)
24. Siegel, A.E.: The Theory of High Speed Guns. AGARDograph, p. 91 (1965)
25. Jackson, S.I., Shepherd, J.E.: The Development of a Pulse Engine Simulator Facility. GALCIT Report FM 2002.006 (2002)
26. Harlow, F., Amsden, A.: Fluid Mechanics. Technical Report. Los Alamos National Laboratories. LANL Monograph LA-4700 (1971)

27. Saito, T., Marumoto, M., Yamashita, H., Hosseini, S.H.R., Nakagawa, A., Hirano, T., Takayama, K.: Experimental and numerical studies of underwater shock wave attenuation. Shock Waves **13**, 139–148 (2003)
28. Jones, D.M., Martin, P.M.E., Thornhill, C.K.: A note on the pseudo-stationary flow behind a strong shock diffracted or reflected at a corner. Proc. R. Soc. Lond. A **209**, 238–248 (1951)
29. Ben-Dor, G.: A state-of-the-knowledge review on pseudo-steady shock-wave reflections and their transition criteria. Shock Waves **15**, 277–294 (2006)
30. Chapman, C.J.: High Speed Flow. Cambridge University Press, Camebridge (2000)
31. Bilaniuk, N., Wong, G.: Speed of sound in pure water as a function of temperature. J. Acoust. Soc. Am. **93**, 1609–1612 (1993)
32. Bilaniuk, N., Wong, G.: Erratum: Speed of sound in pure water as a function of temperature. J. Acoust. Soc. Am. **99**, 3257 (1996)
33. Pianthong, K., Takayama, K., Milton, B.E., Behnia, M.: Multiple pulsed hypersonic liquid diesel fuel jets driven by projectile impact. Shock Waves **14**, 73–82 (2005)